Photocatalytic hydrogen production using mesoporous TiO$_2$ doped with Pt

J.F. Guayaquil-Sosa [a], Benito Serrano-Rosales [c], P.J. Valadés-Pelayo [b], H. de Lasa [a],*

[a] Western University, Faculty of Engineering, Chemical Reactor Engineering Centre (CREC), London, ON, Canada
[b] Instituto de Energías Renovables, Universidad Nacional Autónoma de México, Privada Xochicalco S/N, Col. Centro, Temixco, 62580 Morelos, México
[c] Universidad Autónoma de Zacatecas, Facultad de Ciencias Químicas, Zacatecas, Zacatecas, México

ABSTRACT

A series of mesoporous TiO$_2$ (meso-TiO$_2$) were synthesized using the sol-gel technique. A *Pluronic F127* triblock-copolymer, a structure-directing agent, was incorporated as a soft template into the sol-gel. In addition, and during a separate synthesis, the sol-gel was doped with a Pt precursor. Semiconductors were prepared with 1.00 wt.%, 2.50 wt.%, 5.00 wt.% Pt nominal loadings, respectively. They were calcined at 500 °C and 550 °C following synthesis. Morphological and structural properties were studied by: a) X-ray diffraction, b) UV–vis spectrophotometry, c) N$_2$ adsorption-desorption (BET, BJH), and d) X-ray photoelectron spectroscopy (XPS). Optical band gap values for meso-TiO$_2$ and Pt-meso-TiO$_2$ were calculated by *Kubelka-Munk (K-M)* function coupled with Tauc plot methodology. It was observed that the prepared semiconductors displayed pore sizes in the 10–40 nm range with bimodal distributions. Their photocatalytic activity for hydrogen production via water splitting was established in a *Photo-CREC Water-II* reactor under near-UV light irradiation. The aqueous solution contained 2% v/v ethanol, employed as a renewable organic scavenger. The prepared semiconductors showed that the mesoporous 2.50 wt.% Pt-TiO$_2$ has the highest photoactivity for hydrogen generation. This suggests the important role played by the loading of platinum as a TiO$_2$ dopant, reducing the optical band gap, increasing electron storage and diminishing, as a result, electron-hole recombination. The measured Quantum Yield (QY), obtained using a rigorous approach, was established for the mesoporous 2.50 wt.% Pt-TiO$_2$ at a promising level of 22.6%.

© 2017 Elsevier B.V. All rights reserved.

1. Introduction

Currently, fossil energy resources are used extensively to satisfy most of the world's energy requirements. Projection of energy use and availability suggests that in the near future, there will be major issues and challenges to be faced with energy supply and demand. Additionally, combustion of fossil fuels leads to atmospheric emissions of carbon particles, CO$_2$ and noxious gases such as NO$_x$, SO$_x$. Thus, environmentally friendly fuels, that are both cost-effective and easily storable, are of great importance for the world's sustainable development [1].

Hydrogen is, in this respect, an ideal candidate as an energy vector [2]. Numerous technologies can be used to generate hydrogen. However, only a few of them can be considered as truly environmentally friendly. Steam hydrocarbon reforming is the current dominant technology for hydrogen production. It requires high temperatures (700–1100 °C) and emits large amounts of CO$_2$ [3]. Hence, efforts focused on water splitting are of great potential significance. Water splitting using solar energy is one of the most attractive approaches to produce hydrogen. Water splitting is an eco-friendly process that can be operated at ambient temperature and pressure. This process can take advantage from sunlight; an abundant and inexpensive renewable energy source [4–6].

The most important issue still to be addressed is the low quantum efficiency of photocatalytic materials in photocatalytic hydrogen production. This is related with restrictions in band gap excitation as well as recombination of charge carriers in semiconductor photocatalysts. Thus, promoting to low hydrogen evolution rates, which up to date have limited the practical application of this technology on a large scale.

In photocatalytic water splitting, photons are absorbed by semiconductors, and as a result, water splits into hydrogen and oxygen. Nevertheless, water splitting is not thermodynamically favourable. Current research focuses on increasing both the efficiency and

* Corresponding author.
  E-mail address: hdelasa@eng.uwo.ca (H. de Lasa).

Nomenclature

c	Speed of light (3.0×10^8 m/s)
C	Celsius
d_p	Porous diameter (cm)
e^-	Electron
h^+	Hole
h	Planck's constant (6.63×10^{-34} J/s)
E	Energy of a photon at a given wavelength (J)
$\bar{E}$	Average energy of a photon at a wavelength range, (J/mol photon)
E_{bg}	Energy band gap (eV)
eV	Electron volts
H_2PtCl_6	Hexachloroplatonic acid
H	Hydrogen radical dot
P_a	Rate of absorbed photons by semiconductor (photons/s)
P_{bs}	Rate of backscattered photons flying off the system (photons/s)
P_i	Rate of photons reaching the reactor inner surface (photons/s)
P_t	Rate of transmitted photons (photons/s)
Pt	Platinum
QY	Quantum yield (%)
R	Rutile
t	Time (h)
TiO_2	Titanium dioxide
V_g	Volume of the gas phase in the storage tank (cm^3)
W	Weight (g)
wt.%	Weight percent (% m/m)

Greek symbols

α	*absorbance* (a.u.)
θ	*diffraction angle* (°)
λ	*wavelength* (nm)
Δ	*Anatase*
ν	*frequency* (1/s)

Acronyms

BJH	Barrett-Joyner-Halenda model
BLB	Black light blue lamp
BET	Brunauer-Emmet-Teller surface area method
CB	Conduction band
DP25	TiO2 degussa P25
Meso	Mesopores
PCWII	Photo CREC water II reactor
QY	Quantum yield
UV	Ultra violet
Vis	Visible
VB	Valance band
VUI	Visible utilized irradiation

Subscripts

a	Absorbed photons by the photocatalyst
bg	Band gap
bs	Photons backscattered by the photocatalyst
g	Gas phase
i	Incident photons to the photocatalyst
t	Photons transmitted by the photocatalyst
max	Maximum
min	Minimum

stability of the materials [7,8]. This is essential to achieve the commercialization of this process [9,10].

Semiconductors are characterized by two types of mobile carriers: a) electrons in the conduction band and b) holes in the valence band. Both bands are separated by an energy gap. There is a continuous transition of electrons between bands. When a valence electron is given an energy equal or greater than the energy band gap, it is transferred to the conduction band, leading to a pair electron-hole formation. When an electron falls from the conduction band into the valence band, and into a hole, a recombination occurs.

Among the various semiconductors, TiO_2 has been extensively studied due to its photosensitivity, low cost, low toxicity, and good chemical and thermal stability. There are two main issues with TiO_2. On one hand, TiO_2 can be activated mainly by near ultraviolet irradiation (near-UV) due to its wide band gap (3.20 eV for anatase and 3.00 eV for rutile), which limits its practical efficiency while using solar energy. In addition, near-UV radiation makes up only 4–5% of the solar spectrum, further reducing its potential applications. On the other hand, a high electron hole recombination reduces the photoelectric conversion efficiency of TiO_2. This being one of the main limitations to the practical application of photocatalysis as a viable technology for solar light harvesting [11–32].
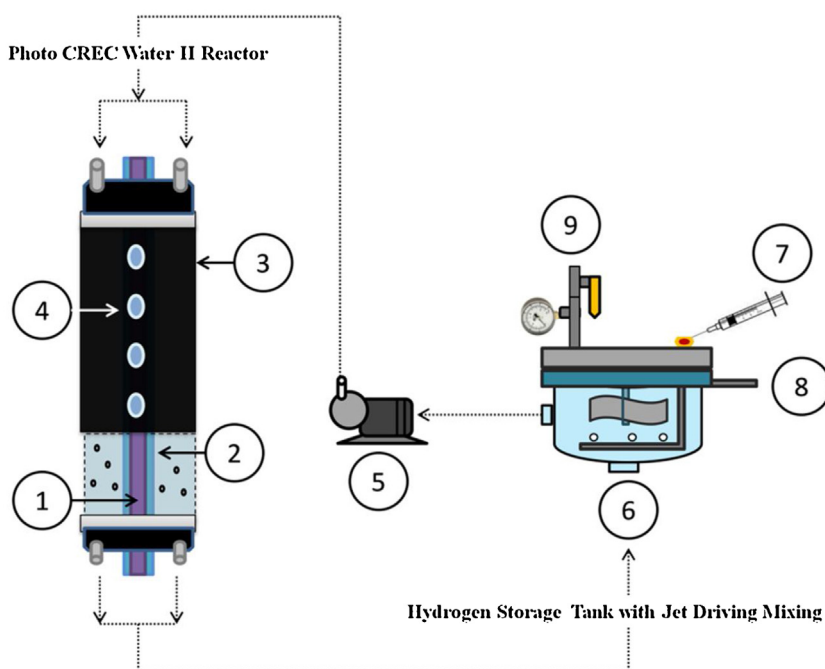
TiO_2 can be modified with CdS, ZnO, PbS, Cu_2O, Bi_2S_3, and CdSe forming TiO_2 composites. Theoretically combining n-type TiO_2 with p-type semiconductors is effective in improving the photoelectric TiO_2 conversion efficiency. Many of these modified materials have received less attention due to, under illumination in contact with water, they can experience photocorrosion (e.g. Zn^{2+} or Cd^{2+} dissolution) [45,47]. A reliable alternative to improving photoelectric conversion is the addition of noble metals (e.g. Pt, Au, Ag and Pd) during the semiconductor synthesis. Noble metals addition favours water splitting given the separation of photoproduced electron-hole pairs because: a) the surface plasmon resonance of noble metal particles can be excited by visible light, (b) the energy band gap is reduced, and c) the noble metal nanoparticles act as electron traps [46].

CREC-UWO research group developed a platinum modified TiO_2 photocatalyst [33–36]. Pt modified photocatalysts were evaluated in a *Photo-CREC Water-II (PCWII)* Reactor using 2% v/v ethanol water acidic solutions (pH = 4.00 ± 0.05) under near-UV light irradiation [36]. Low grade ethanol is a renewable carbon containing scavenger. Dissociated water and photon activated semiconductors yield H• and OH•. Pairs of H• radicals combine forming H_2, while the ethanol OH• scavenger forms CO_2, CH_4 and C_2H_6. Under oxygen-free conditions, Quantum Yields (QY) as high as 8% were obtained. Hydrogen was produced in a stable process with no detectable photocatalyst deactivation [36].

The present study considers the use of mesoporous TiO_2 with high specific surface area. It is postulated that the high expected mesoporous TiO_2 photocatalytic activity can be enhanced with noble metals, such as Pt. Moreover, Pt can trap photogenerated conduction electron, and electron acceptor H^+ obtains the electron in order to produce hydrogen on Pt [38–44]. Furthermore, these noble metals display high Schottky barriers and thus favouring electron trapping and charge separation. To demonstrate high photoactivity with noble metals, the performance of these semiconductors should be ranked with a rigorous evaluation of QY.

2. Photocatalyst engineering

A phenomenological approach for photocatalyst design for hydrogen production involves the followings: a) Semiconductor purity: the highest possible anatase content close to 100%. This appears to enhance under concurrent conversion of an ethanol scavengers, hydrogen production, a) Surface area of the meso-

Fig. 1. Schematic diagram of the *Photo-CREC-Water-II* photoreactor with a H_2 mixing tank: (1) BLB lamp, (2) Pyrex glass tube, (3) UV-opaque polyethylene cylinder, (4) fused-silica windows, (5) centrifugal pump, (6) H_2 storing/mixing tank, (7) gas sampling port, (8) purging gas injector and (9) draining gas valve. Adapted from [36].

porous TiO_2: the highest possible. This can be accomplished with a mesoporous TiO_2 with a regular and nanometric pore sizes, c) Crystallite size: the smallest possible with Pt crystallites, consistent with the pore sizes and pore volume of the synthesized mesoporous TiO_2. This can lead to a nanometric Pt crystallites and high Pt metal dispersion.

3. Preparation of mesoporous titania nanoparticles

The copolymer surfactant $-CH_2CH_2O_{-106}$-$CH_2(CH_3)CHO$-$_{70}$-$CH_2CH_2O_{-106}$ (*Pluronic F127*, M_{AVG} = 12600) was used as a structure-directing template. Hydrochloric acid of 37% purity, as well as citric acid and titanium (IV) isopropoxide (Sigma Aldrich $Ti(OC_3H_7)_4$), were employed as co-reactants.

In a typical synthesis, 400 mL of ethanol (CH_3CH_2OH) from Commercial Alcohols (A Trade Name of Greenfield Specialty Alcohols) were acidified with 33.00 g of hydrochloric acid (37 wt.% purity). After combining these reagents, 20.00 g of *Pluronic F127* were added, and the suspension was mixed until dissolution (*0.5* h). Then, 6.30 g of citric acid were incorporated under intense stirring. Following this procedure, the solution pH was adjusted to 0.75. Mixing continued at ambient temperature for 1 h. Once this step was completed, 28.50 g of titanium (IV) isopropoxide were poured dropwise. The resultant liquid phase, displaying a sol-gel appearance, was mixed for 24 h. At the end of this period, it was split in two equal solutions, labelled A and B. The resulting sol-gel phases were evaporated and calcined by gradually increasing the temperature, from room temperature to 773 K (500 °C) for flask A and to 823 K (550 °C) for flask B at a 1 °C/min heating rate. Once the desired thermal level was reached (i.e. 773 K for A and 823 K for B), this temperature was kept during 6 h under ambient air to calcine the sample and combust the organic template.

Synthesis conditions selected secured template-free self-assembled mesoporous titania nanoparticles. Samples obtained following this process were labelled as TiO_2- Meso–500 °C and TiO_2- Meso–550 °C, respectively.

Given the importance of doping TiO_2 with Pt for water splitting [36], the synthesized mesoporous titania of the present study, was also doped with platinum incorporated into the TiO_2 lattice. Titanium (IV) isopropoxide template method was modified with the used of hexachloroplatinic acid hydrate (Sigma Aldrich H_2PtCl_6*xH_2O). Titanium (IV) isopropoxide was added in the sol-gel concurrently with the Pt containing species.
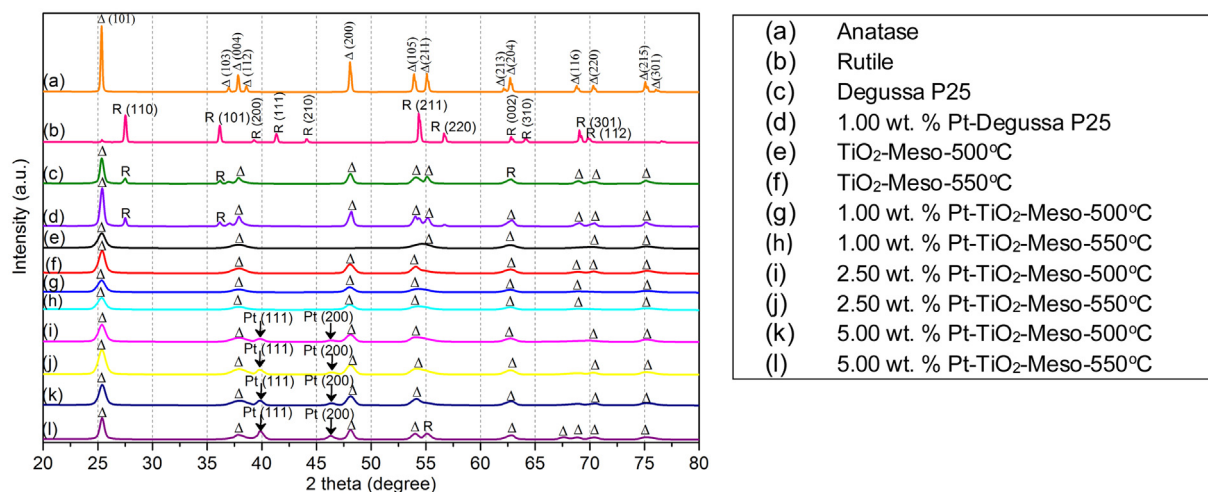
Prepared samples using the above described steps were designated as: a) 1.00 wt.% Pt-TiO_2-Meso–500 °C and 2.50 wt.% Pt-Meso-TiO_2–500 °C and b) 1.00 wt.% Pt- TiO_2- Meso–550 °C, and 2.50 wt.% Pt-TiO_2- Meso–550 °C.

4. Photocatalytic performance

The photocatalytic activity of the synthesized semiconductors was determined using a *Photo-CREC Water-II* bench scale photoreactor *(PCWII)* [36] containing a hydrogen storage tank with jet driving mixing. *PCWII* is comprised of a 2.65 L internally irradiated slurry annular section and a total 6.00 L slurry volume. A 15 W EIKO T8 Black-Light-Blue (BLB) lamp is the light source. This lamp displays a wavelength peak at 370 nm and emits in the range of 320 nm–410 nm. The photocatalyst loading was evaluated in the range 0.05–1.00 g/l in an acid medium (pH = 4.00 ± 0.05). A 1.00 g of TiO_2/Liter loading was used with Pt embedded in the mesoporous TiO_2. This was done to ensure that a 90% of the incident energy was absorbed in all experiments. Absolute ethanol was used as a renewable organic scavenger. Ethanol was kept at 2% v/v as reported in our previous studies [36].

5. Experimental set up

Fig. 1 reports a description of the *Photo-CREC Water-II* reactor with the following components: (1) 15-W black light lamp or (BLB), (2) Pyrex glass inner tube with a 3.58 cm diameter, (4) silica windows, (5) black polyethylene outer tube, (6) stirred tank, (7) centrifugal pump, (8) purging gas injector, and (9) sampling port. 15-W lamp, 1.33 cm radius, 41.3 cm length, black-light UV lamp is

Fig. 2. XRD diffractograms of the photoactive materials for hydrogen production. XRD diffractograms were overlapped for comparison. (Δ) represents TiO_2 in the anatase phase and (R) indicates TiO_2 in the rutile phase.

positioned at the center of the inner Pyrex tube, which was selected given its high irradiation transmittance.

6. XRD diffractograms

Powder XRD spectra were taken on using a Rigaku Rotating Anode X-Ray Diffractometer employing CoKa radiation. The instrument was operated at 45 kV and 160 mA. X-rays were collimated using 1° divergent and scatter slits, and a 0.15-mm receiving slit. Continuous scans were collected over the 2θ range 20–80° with a step size of 0.02° for a dwell time of 2 s per step.

One can observe in Fig. 2 that the characteristic crystalline phases for TiO_2 are also present in the mesoporous TiO_2 calcined at 500 °C and 550 °C, respectively. Fig. 2 also provides XRD for other TiO_2-based photocatalysts doped with platinum, curves (g)–(l). For those cases, the characteristic anatase peaks at the 2θ diffraction angles of 25, 38, 48, 54, 63, 69, 70.5 and 75° corresponding to the planes (101), (004), (200), (105), (204), (116), (220) and (215) were consistently observed. Fig. 2(d) shows small extra peaks for the 1.00 wt.%-Pt-Degussa P25 at 27, 36, 55.1 and 57° corresponding to the rutile phase in the planes (110), (101), (211) and (220) respectively.

Furthermore, the XRD diffractograms of Fig. 2(i)–(l), for the loadings of 2.50 and 5.00 wt.% platinum, in the mesoporous TiO_2, report an extra peak at 47° in the 2θ scale. This can be attributed to the Pt, which modifies the TiO_2 with an extra crystalline phase. An interesting observation is that when increasing the Pt loading, the 47° peak augments in intensity. Close examination of the peaks in Fig. 2(i)–(l), reveals that two of them occurred for the samples with Pt. These peaks can be attributed to the (111) and (200) reflections of the Pt° (JCPDF 01-1194) possessing a face-centered cubic structure. These peaks are weak and broad, indicating the nanocrystalline nature of the Pt particles.

Fig. 2 also shows the effect of the Pluronic and the Pt loading on the TiO_2. It is shown that the *Pluronic F127*-modified mesoporous TiO_2 displays a lower crystallinity than that non-porous TiO_2 (i.e. 1.00 wt.%-Pt/Degussa P25). However, the addition of the Pt increases crystallinity of the mesoporous TiO_2. Moreover, an increase in Pt loading leads to higher XRD intensities with a narrowing of the (111) peak, indicating a progressive growth of crystallites.

Table 1 reports the crystallite sizes for several TiO_2 used, as calculated with the Scherrer equation. The synthesized mesoporous TiO_2 displays 8–11 nm crystallite sizes. This is in contrast with the

Table 1
Crystallite sizes of mesoporous TiO_2, Pt-TiO_2 with different Pt loadings.

Photocatalyst	Crystallite size[a] (nm)
Meso-TiO₂–500 °C	8
Meso-TiO₂–550 °C	8
1.00 wt.% Pt/Meso-TiO₂–550 °C	10
2.50 wt.% Pt/Meso-TiO₂–550 °C	10
5.00 wt.% Pt/Meso-TiO₂–550 °C	11
1.00 wt.% Pt/Degussa P25	22
Degussa P25	21
Anatase	48
Rutile	51

[a] XRD-method.

21–22 nm for the Degussa P25 and the 48, 51 nm for anatase and rutile, respectively.

7. N_2 adsorption-desorption isotherms of mesoporous TiO_2

In order to establish the structural differences, potentially affecting the photocatalytic activity for hydrogen formation from water splitting, the synthesized mesoporous TiO_2 were analyzed using N_2 adsorption-desorption isotherms and BET method. Nitrogen adsorption and desorption isotherms at −195 °C were measured using a Micrometrics ASAP-2010 specific surface area and porosity analyzer. This was accomplished once the mesoporous TiO_2 samples were degassed in a vacuum at 250 °C for 2 h. Figs. 3 and 4 report typical examples of the nitrogen adsorption-desorption isotherms obtained in the present study.
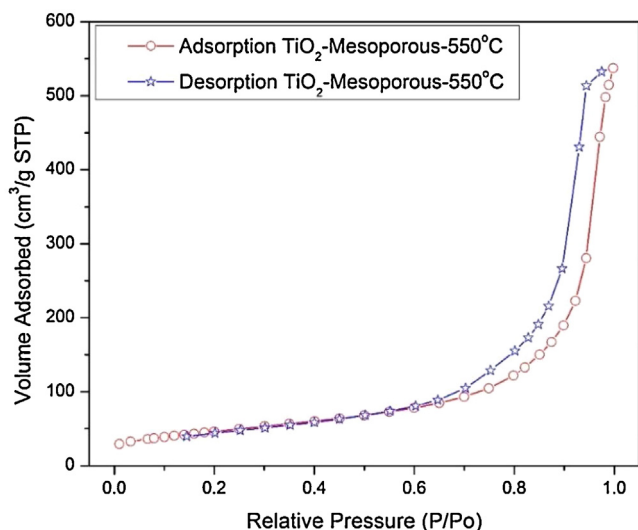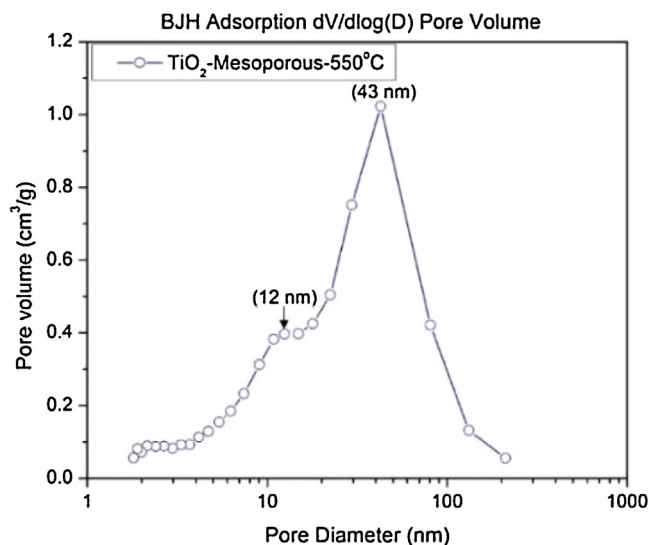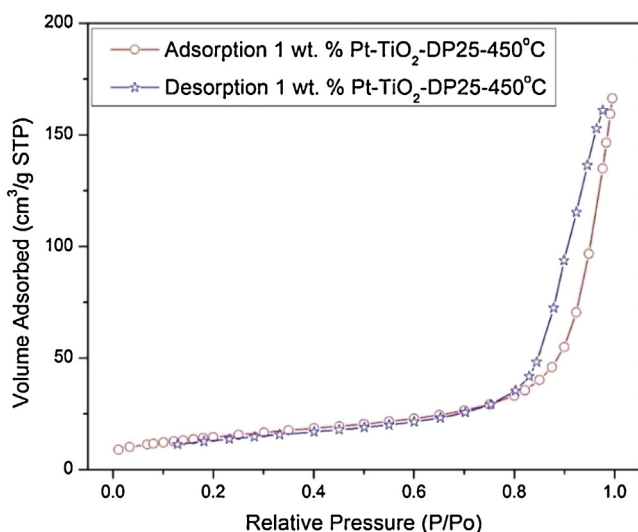
Adsorption-desorption isotherm of the synthesized mesoporous materials (Fig. 3) belongs to a Type IV classification [55–57]. This isotherm features a hysteresis loop, associated with capillary condensation in the mesopores, and a limited nitrogen uptake over a range of high *P/Po*. The initial branch of the isotherm is attributed to a monolayer coverage. Type IV isotherms are found in many mesoporous industrial adsorbents [58].

Additionally, metal dispersion was calculated by pulse chemisorption analysis using a Micrometrics, AutoChem II 2920 V 4.00 unit. Through the hydrogen chemisorption analysis one can speculate that the well-dispersed metal particles onto mesoporous TiO_2 surface may improve the electron surface distribution.

The specific surface area was calculated using the Brunauer-Emmett-Teller (BET) plot. As shown in Table 2, typical values obtained for the mesoporous TiO_2 were in the 130–170 m²/g range. This was significantly higher than the 50 m²/g for the commercial

Table 2
Specific surface area, pore volume and pore diameter for different photocatalyst materials. Also, metal dispersion for mesoporous TiO_2 materials is reported.

Photocatalyst	$S_{BET}(m^2\,g^{-1})$	$V_p^{BJH}(cm^3\,g^{-1})$	$D_p^{BJH}(4\,V_p^{BJH}/S_{BET})$ (nm)	MetalDispersion(%)
Meso-TiO$_2$–550 °C	168	0.68	16.19	N/A
1.00 wt.% Pt/Meso-TiO$_2$–550 °C	136	0.45	13.24	54.2
2.50 wt.% Pt/Meso-TiO$_2$–550 °C	150	0.68	18.13	45.7
5.00 wt.% Pt/Meso-TiO$_2$–550 °C	155	0.66	20.07	25.7
1.00 wt.% Pt/Degussa P25	52	0.21	16.15	N/A
Degussa P25	50	0.25	20.00	N/A
Anatase	8	0.05	25.00	N/A
Rutile	7	0.05	28.57	N/A

Fig. 3. N$_2$ adsorption-desorption isotherm of mesoporous TiO$_2$ semiconductor calcined at 550 °C.

Fig. 5. Barrett-Joyner-Halenda (BJH) pore size distribution plot of mesoporous TiO$_2$ calcined at 550 °C.

Fig. 5 shows a bimodal pore size distribution plot. This bimodal pore volume distribution was consistently observed for the following TiO$_2$ based materials: a) Meso-TiO$_2$–500 °C, b) Meso-TiO$_2$-550 °C, c) 1.00 wt.%-Pt-Meso-TiO$_2$–500 °C, d) 1.00 wt.%-Pt- Meso-TiO$_2$–500 °C, e) 1.00 wt.%-Pt-Meso-TiO$_2$–550 °C, f) 2.50 wt.%-Pt-Meso-TiO$_2$–500 °C. These distributions display pore sizes belonging to both 12–15 nm range and 30–46 nm range.
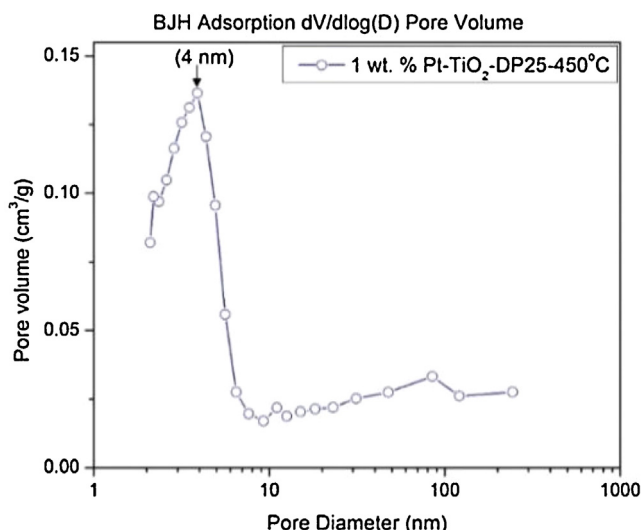
Only one TiO$_2$-based material studied displayed a single pore size distribution, as shown in Fig. 6. This was found on the 1.00 wt.%-Pt- Degussa P25–450 °C. Average pore sizes were in the 4-nm range.

8. X-ray photoelectron spectroscopy (XPS)

X-ray photoelectron spectroscopy (XPS) experiments were performed to investigate: a) the concentration of the titanium and platinum in the mesoporous titania, b) species oxidation state and c) their effect on the semiconductor structure (Fig. 7a and b).

The survey spectra for all samples exhibited strong XPS peaks for titanium and oxygen. On this basis meso-TiO$_2$ powders were examined and this to assess the amount of Ti^{3+} versus Ti^{4+} ions. Moreover, the chemical state of platinum on the photocatalyst surface was also investigated with platinum species displaying moderate XPS peaks. Additional discussion of the XPS spectra obtained for the Pt-TiO$_2$ photocatalyst are reported in Appendix I.

Evidence suggests that synthesis conditions influence TiO$_2$ structural properties. Synthesis conditions must be carefully controlled during photocatalyst synthesis to achieve adequate pore size distribution and high specific surface area. Thus, a successful photocatalyst design with adequate properties for hydrogen production, should encompass key synthesis steps as follows: a) The preparation of 10–40 nm mesoporous TiO$_2$ with carefully sized
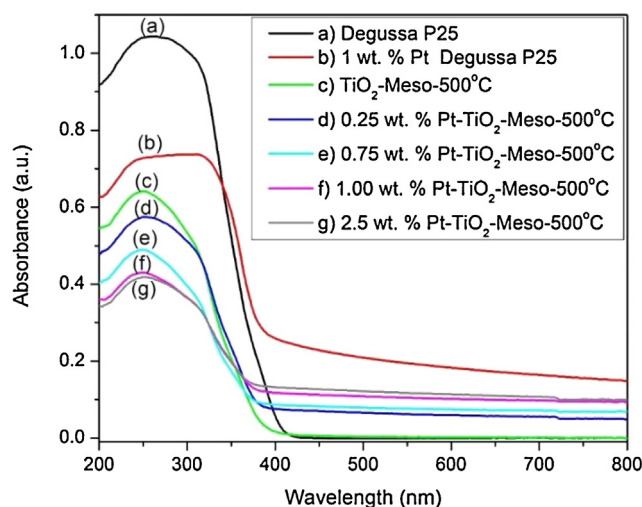

Fig. 4. N$_2$ adsorption-desorption isotherm of 1.00 wt.%-Pt/Degussa P25 heated at 450 °C.

Degussa P25 and compared to the 7–8 m^2/g for anatase and rutile, respectively.

In addition, pore size distributions were calculated by employing the Barrett-Joyner-Halenda (BJH) model. The pore volume was measured at P/Po = 0.99. Helium gas was used for dead region measurements, whereas nitrogen was utilized to establish sorbed gas.

Fig. 5 reports the Barrett-Joyner-Halenda (BJH) pore size distribution plots, for the synthesized mesoporous semiconductor calcined at 550 °C.

Fig. 6. Barrett-Joyner-Halenda (BJH) pore size distribution plot of 1.00 wt.%-Pt-TiO$_2$ Degussa P25 semiconductor heated at 450 °C.

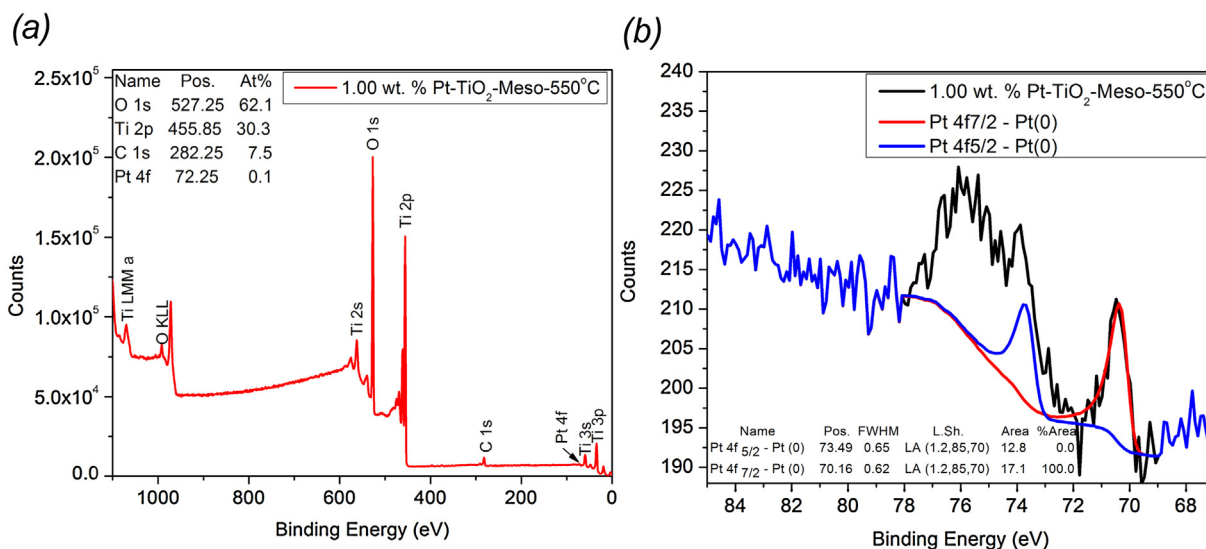**Fig. 8.** UV–vis absorption spectra of the different semiconductor materials calcined at 500 °C: a) Degussa P25, b) 1.00 wt.% Pt / Degussa P25-450 °C, c) Meso-TiO$_2$, d) 0.25 wt.% Pt- Meso-TiO2, e) 0.75 wt.% Pt- Meso-TiO$_2$, f) 1.00 wt.% Pt- Meso-TiO2 and g) 2.50 wt.% Pt- Meso-TiO$_2$.

pores. This can be accomplished using sol-gel synthesis and a wisely selected organic template, b) The addition of a platinum precursor in an acidic medium to achieve high platinum dispersion. This can be attained using a stable platinum containing platinic species under acidic conditions, c) The use of a moderate 500–550 °C calcination temperature. This leads to Pt in the metallic state directly, and eliminates the requirement of further reduction steps of the photocatalyst.

9. Band gap

UV–vis spectra of the photocatalysts in solid phase were recorded by a *UV–vis-NIR* spectrophotometer (Shimadzu UV 3600) equipped with an integrating sphere using *BaSO$_4$* as a reference.

Determination of semiconductor optical band gap is required to determine wavelengths that activate the photocatalyst. To this end, the Kubelka-Munk (K-M) function and the Tauc plot method was used [48]. "Indirect band gap" data treatment designated as the Kubelka-Munk (K-M) and a Tauc plot is highly recommended for the synthesized photocatalysts [49,50].

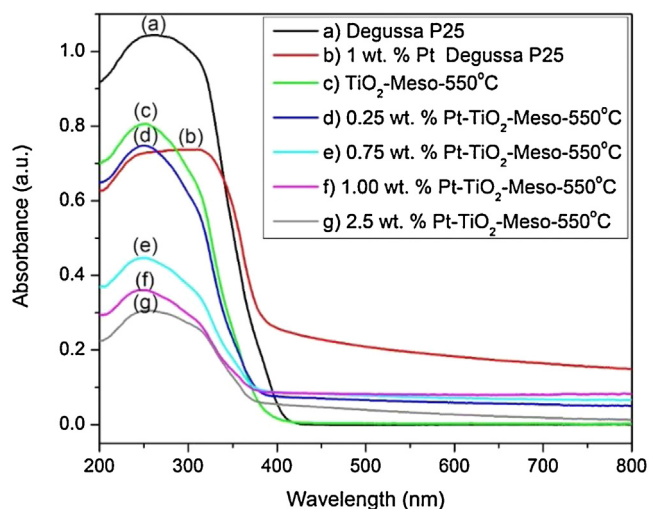Fig. 8 reports the UV–vis spectra at various wavelengths, reported at 500 °C for different loadings of platinum.

Fig. 8 shows that the commercial TiO$_2$ (Degussa P25) displays the highest absorbance values, whereas the prepared mesoporous materials (Meso-TiO$_2$), consistently gives lower absorbance. This shows as well, that Pt loading influences the UV–vis spectra, with reduced absorbance for increased platinum loadings.

Furthermore, considering the straight-line approximation and the intersection with the abscissa axis, one can determine larger wavelengths at zero absorbance or the equivalent, a band gap reduction with increased Pt. This finding agrees with the XRD measurements described above, showing new crystalline phases with Pt addition.
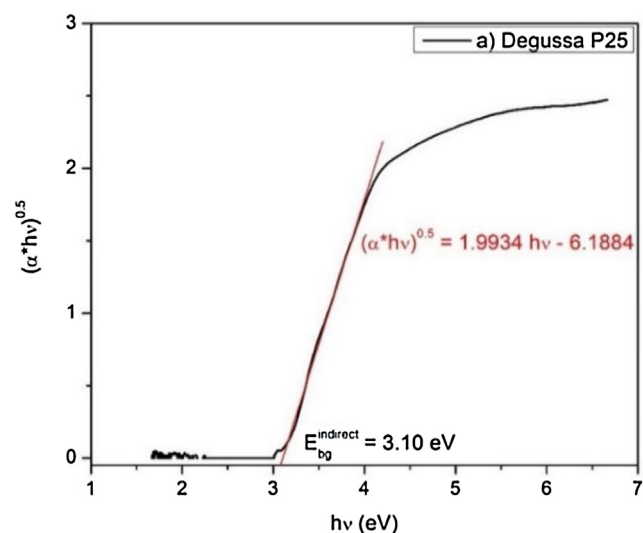
Fig. 9 reports the UV–vis absorbance as a function of the wavelength for the photocatalyst calcined at 550 °C, an increased wavelength at zero absorbance for both Meso-TiO$_2$ and Meso-TiO$_2$ with loaded Pt is observed.

Fig. 7. X-ray photoelectron spectroscopy (XPS) of 1.00 wt.% Pt-mesoTiO$_2$−550 °C. (a) XPS survey and (b) High-resolution XPS spectrum.

Fig. 9. UV–vis absorption spectra of the different semiconductor materials calcined at 550 °C: a) Degussa P25, b) 1.00 wt.% Pt/Degussa P25–450 °C, c) Meso-TiO$_2$, d) 0.25 wt.% Pt- Meso-TiO$_2$, e) 0.75 wt.% Pt-Meso-TiO$_2$ f) 1.00 wt.% Pt-Meso-TiO$_2$ and g) 2.50 wt.% Pt- Meso-TiO$_2$.

Fig. 11. Optical band gap calculation for Meso-TiO$_2$–550 °C using the Tauc plot. This plot was established using the UV–vis absorption spectra. Calculated indirect band gap = 2.99 eV.
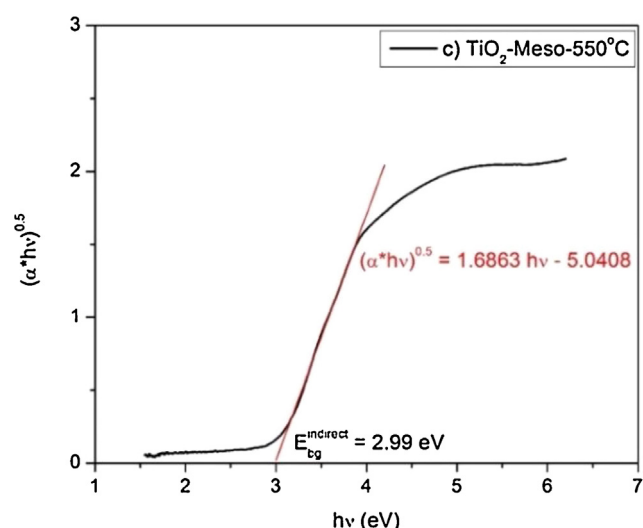

Fig. 10. Optical band gap calculation for Degussa P25 (DP25) using the Tauc plot method. This plot was established using the UV–vis absorption spectra. Calculated indirect band gap = 3.10 eV.

Fig. 12. Optical band gap determination for a 2.50 wt.% Pt-Meso-TiO$_2$–550 °C using the Tauc Plot. This plot was established on the basis of the UV–vis absorption spectra. Calculated indirect band gap = 2.34 eV.

Regarding the optical band gaps, the Kubelka-Munk (K-M) function coupled with "indirect" procedure (Tauc plots) was adopted as follows:
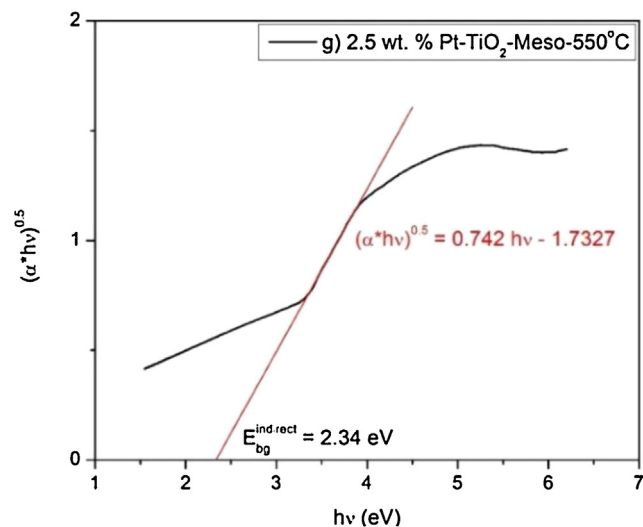
a) The $\sqrt{\alpha h\nu}$ variable was selected for the "y" ordinate, with α representing the UV-vis absorbance.
b) The $h\nu$ variable was chosen for the "x" abscissa, with h being the Planck constant (6.63×10^{-34} Joule/s), c denoting the light speed (3.0×10^8 m/s) and $\nu = \frac{c}{\lambda}$ representing the irradiation frequency.

On this basis, Tauc plots as in Figs. 10–12 were obtained.

Regarding the Tauc plots method, as in Fig. 10, the linear section close to the inflection point region has to be considered according to the Tauc plots method. The resulting straight line provides the equation $(\alpha * h\nu)^{\frac{1}{2}} = 1.9934 (h\nu) - 6.1884$, with a 0.996 regression coefficient. Furthermore, the intersection of this straight line with the abscissa axis at $(\alpha * h\nu)^{\frac{1}{2}} = 0$, yields $E_{bg} = h\nu$, 1.9934 $(E_{bg}) - 6.1884 = 0$ and $E_{bg} = 6.18/1.99 = 3.10$ eV.

A similar analysis is developed in Figs. 11 and 12, for the cases of Meso-TiO$_2$–550 °C and 2.50 wt.% Pt-Meso-TiO$_2$–550 °C. The band gaps are 2.99 eV and 2.34 eV, respectively.

Figs. 13 and 14 describe the influence of platinum loading on the optical band gaps for the semiconductors synthesized in this work.

Tables 3 and 4 report a comparison of various band gaps for the materials of the presents study, showing the progressive reduction with the increased Pt loadings.

Tables 3 and 4 report the optical band gaps for commercial TiO$_2$ (Degussa P25) and Meso-TiO$_2$–500 °C and Meso-TiO$_2$–550 °C. These results show that the TiO$_2$ architecture has an effect on band gaps, with this being assigned to the higher anatase content of the mesoporous TiO$_2$. Both Tables 3 and 4 also show that the band gap is consistently reduced by the Pt loading.

One can notice that there is a consistent band gap reduction with platinum loading. Furthermore, the higher calcination temperature of 550 °C, provides a slightly enhanced λ_{bg}.

Thus, on the basis of the above, one can conclude that the platinum added mesoporous materials are able to more effectively use
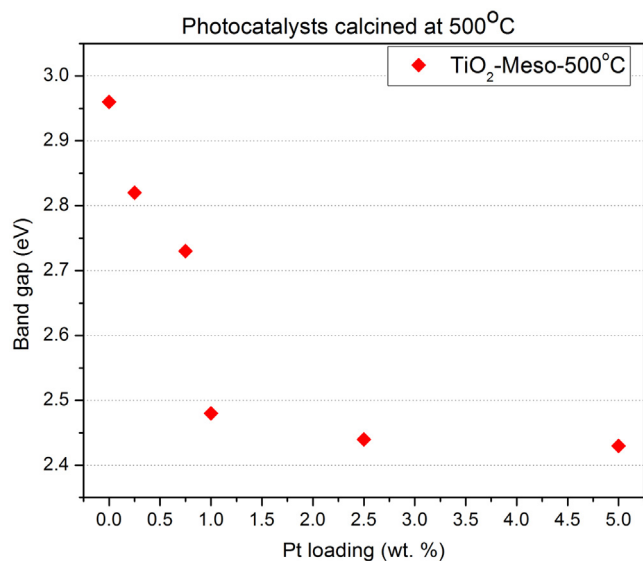
Table 3
Optical band gap of materials calcined at 500 °C, calculated with the Kubelka-Munk (K-M) function and Tauc plot method.

Semiconductor	Bang gap(eV)	Wavelength associated to the band bap, λ_{bg} (nm)	% of the visible light region absorbed (theoretically) as per Eq. (1)
Degussa P25	3.10	400	0
TiO_2-Meso–500 °C	2.96	419	0
0.25 wt% Pt-TiO_2–500 °C	2.82	440	13.34
0.75 wt% Pt-TiO_2–500 °C	2.73	454	18.00
1.00 wt% Pt-TiO_2–500 °C	2.62	473	24.34
2.50 wt% Pt-TiO_2–500 °C	2.44	508	36.00

Table 4
Optical band gap of materials calcined at 550°, calculated with the Kubelka-Munk (K-M) function and Tauc plot method.

Semiconductor	Bang gap(eV)	Wavelength associated to the band bap, λ_{bg} (nm)	% of the visible light region absorbed (theoretically) as per Eq. (1)
Degussa P25	3.10	400	0
TiO_2-Meso–550 °C	2.99	415	5.00
0.25 wt% Pt-TiO_2–550 °C	2.91	426	8.67
0.75 wt% Pt-TiO_2–550 °C	2.70	459	19.67
1.00 wt% Pt-TiO_2–550 °C	2.59	454	18.00
2.50 wt% Pt-TiO_2–550 °C	2.34	530	43.34

Fig. 13. Effect of the platinum loading on the optical band gap of materials calcined at 500 °C.

Fig. 14. Effect of the platinum loading on the optical band gap of materials calcined at 550 °C.

the visible light. A quantification of this enhanced visible light irradiation can be accounted for using the following equation:
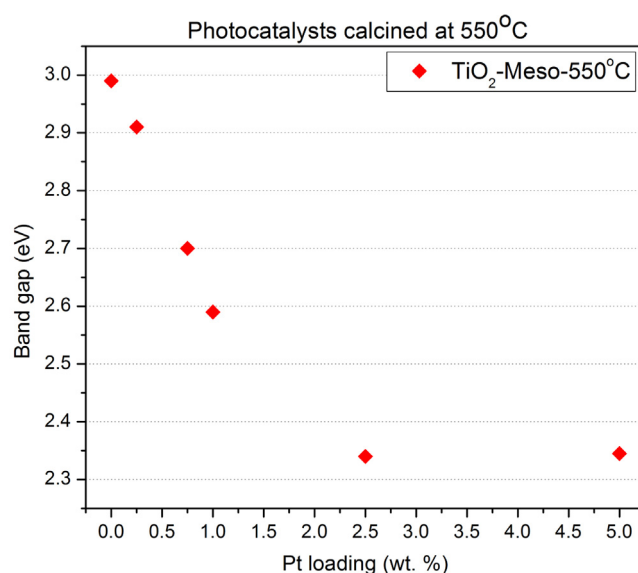
$$Visible\ Utilized\ Irradiation\ \%\ (VUI) = \frac{\int_{\lambda\,min}^{\lambda\,bg} I\,d\lambda}{\int_{\lambda\,min}^{\lambda\,max} I\,d\lambda} x100\% \qquad (1)$$

with I being the irradiance, λ_{min} and λ_{max} representing the minimum and the maximum wavelengths of solar irradiation and λ_{bg} denoting the wavelength associated to the measured optical band gap.

Both Tables 3 and 4 report the expected VUI% which is increased up to 36%–43%, as a result of Pt addition.

10. Scanning electron microscopy (SEM)

SEM micrographs of mesoporous TiO_2 photocatalysts with different Pt loadings are shown in Fig. 15. One can observe, the Pt-TiO_2
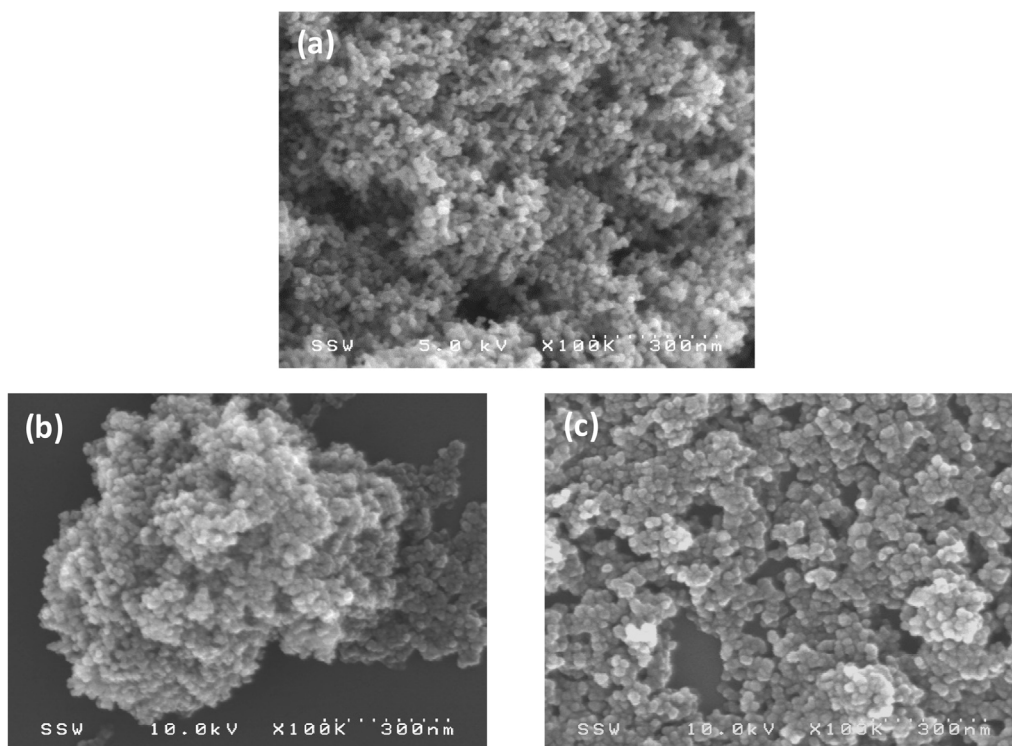
powders under calcination at 550 °C exhibit increased grain and pore sizes. This may be explained due to calcination at 550 °C improved the crystallinity of TiO_2 materials and correspondingly the combustion of *Pluronic F127* promoted increasing pore size.

11. Hydrogen production via water splitting

Experiments of hydrogen formation via photocatalytic water splitting were performed using the *Photo-CREC Water-II* Reactor (refer to Fig. 3). This unit was used with a specially designed H_2 collector tank and a BLB lamp that permits the entire use of the near-UV light irradiation spectrum. 2 v/v% ethanol (EtOH) as a hole (h^+) was employed as a scavenger. This research also took advantage of the mesoporous semiconductor material of TiO_2 and its modifications with Pt conveniently reduced optical band gap.

Experiments in the *Photo-CREC Water-II* Reactor also allowed determining the production of different intermediates and by-products such as: 1) liquid phase: CH_3COOH and 2) gas phase:

Fig. 15. SEM images of mesoporous Pt–TiO$_2$ photocatalysts prepared with different platinum loading at 550 °C calcination temperature. (a) *1.00* wt% *Pt-TiO$_2$–Meso*; (b) *2.50* wt% *Pt-TiO$_2$–Meso*; (c) *5.00* wt% *Pt-TiO$_2$–Meso*.

forms CO_2, CH_4 and C_2H_6 under oxygen free conditions. These were formed during photocatalytic hydrogen generation.

Fig. 16 shows that in all cases, there is a steady hydrogen increase throughout the entire run with no observable photocatalyst activity decay. Experiments in the *Photo-CREC Water-II* Reactor showed a major growth in H$_2$ production when Pt is added in the mesoporous TiO$_2$ at 2.5 wt.%. Hydrogen generation with an ethanol scavenger proceeds consistently via a similar redox network path yielding CH_3COOH, H_2O_2, CH_4, C_2H_6, and CO_2.
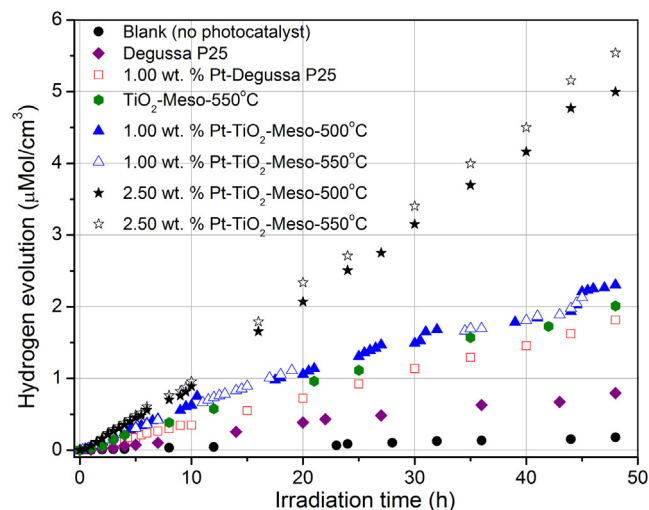
12. Quantum yields (QYs)

The comparison of the performance of TiO$_2$ semiconductors for hydrogen production needs a rigorous assessment of QY [51–54]. The adequate definition of QYs requires macroscopic energy balances allowing Q$_{abs}$ to be measured. The so-called quantum yield is defined as the ratio of the moles of photons effectively converted into products to the moles of absorbed photons. Thus, QY can be calculated as follows:

$$QY = \frac{2\, Moles\, of\, H_2\, Produced/s}{Moles\, of\, Photons\, Absorbed/s} \qquad (2)$$

In this calculation, the photons absorbed (Pa) were calculated using macroscopic balances taking into account for incident, transmitted and reflected photons [36,37]. The number of Einstein effectively converted in hydrogen production can be easily calculated as twice the moles of hydrogen formed, due to two electrons are needed to produce one hydrogen molecule.

A significant increase, from the 7.9% of the previous QY values reported by Escobedo et al. [36], to the 9.6% and to the 22.6% QY values for 1 wt.%-Pt-TiO$_2$-Meso–550 °C and 2.50 wt.%-Pt-TiO$_2$-Meso–550 °C photocatalysts is observed, respectively. These QY enhancements are assigned to the favourable influence of mesoporous architectures of the synthesized semiconductors in the present study.

Fig. 16. Hydrogen evolution for different semiconductor materials at pH = 4.00 ± 0.05 and 2% v/v ethanol. Photocatalyst loading 1.00 g/l. Standard deviation for repeats ± 5%.

Table 5 reports the QY (%) of the semiconductors prepared in this study. The 2.50 wt.%-Pt- TiO$_2$-Meso–550 °C displays a 22.6% QY, about 6 times greater than that for bare DP25 displaying only a 3.5% QY. Appendix II reports additional clarifications concerning the QYs calculations.

Thus, and in the basis of results obtained in the present study, one can establish that doped Pt in mesoporous TiO$_2$, using near UV irradiation and ethanol as a scavenger, can yield considerably enhanced QY for hydrogen production from water splitting. It is our view that the proposed mesoporous TiO$_2$-Pt data may be most valuable for the engineering of scaled up photoreactors for hydrogen production.

Table 5
Quantum yields for mesoporous platinum modified TiO_2, showing the effect of different loadings of Pt with a pH = 4.00 ± 0.05 in the *Photo-CREC Water-II* reactor.
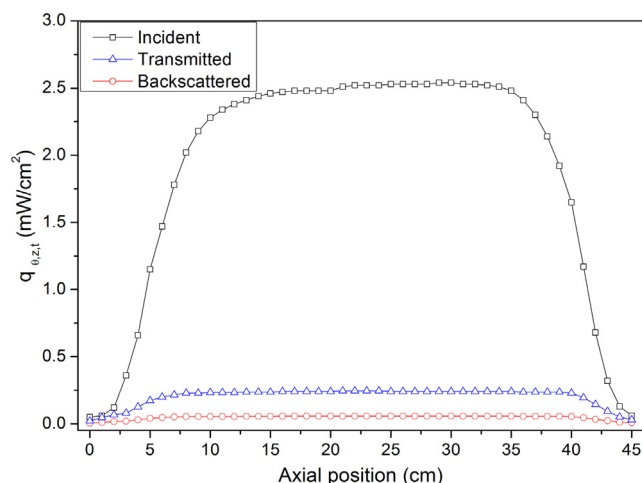
Photocatalyst	QY(%)
Meso-TiO$_2$−550 °C	9.3
1.00 wt% Pt/Meso-TiO$_2$−550 °C	9.6
2.50 wt% Pt/Meso-TiO$_2$−550 °C	22.6
5.00 wt% Pt/Meso-TiO$_2$−550 °C	13.7
1.00 wt% Pt/TiO$_2$ Degussa P25	7.0
Degussa P25 TiO$_2$	3.5
Anatase	N/A
Rutile	N/A

13. Conclusions

a) The mesoporous photocatalysts of the present study, prepared by a sol-gel method, display large surface areas and a bimodal pore size distribution.

b) These mesoporous photocatalysts have a dominant anatase crystalline phase and show a decrease of the band gap with Pt addition.

c) These semiconductors are shown to display a zero-order reaction for hydrogen production with this being true for all photocatalysts studied.

d) Hydrogen formation is proven to increase with Pt loading when using ethanol at 2% v/v concentration. This shows the very important role played by Pt reducing the semiconductor band gap and trapping the electrons generated.

e) The synthesized Pt-mesoporous semiconductors are shown to display promising QYs of 22.6% for the 2.5 wt.% Pt-TiO$_2$-Meso.
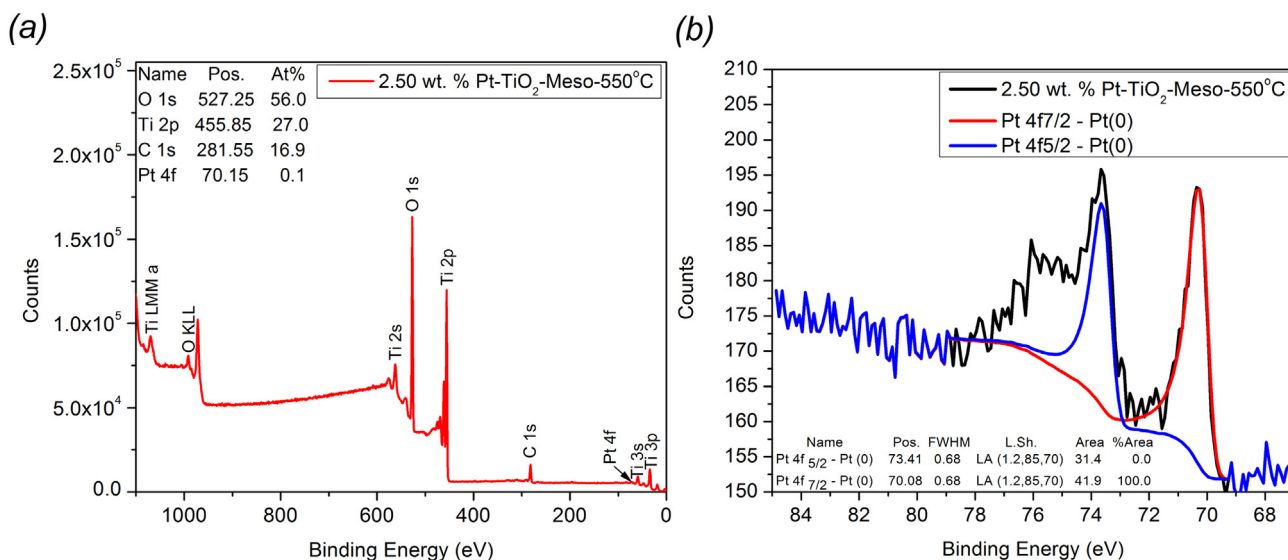
Fig. A2. Radiation distribution along axial position in the *Photo-CREC-Water II* Reactor. Three measurement locations were performed: a) Incident radiation on the mesoporous TiO$_2$ ⊔, b) Transmitted radiation through photocatalyst Δ, and c) Backscattered radiation by the semiconductor ○.

Appendix I. XPS for the Photocatalysts of the Present Study

This appendix provides together with Fig. A1 additional information regarding the XPS analysis for the Photocatalyst of the present study. In particular, Fig. A1 reports photoelectron spectroscopy (XPS) survey for the 2.50 wt.% Pt-mesoTiO$_2$−550 °C.

Regarding XPS it was valuable to establish the electronic state of Pt in the prepared photocatalysts. One can see in Fig. A1(a) the peaks for Ti, O, C, and Pt elements. Regarding the carbon peak, it can be attributed to the residual carbon from the pluronic precursor.

Furthermore, and concerning the Ti2p peak at 455.85 eV, the O1s peak at 527.25 eV and the Pt4f peak at 70.15 eV. These peaks reveal the presence of Ti, O, and Pt elements in Pt–TiO$_2$. Fig. A2 shows the high-resolution XPS spectra in the 67–85 eV range. These findings confirm the presence of Pt, as Pt4f$_{7/2}$ at 70.05 eV and Pt4f$_{5/2}$ at 73.41 eV). There is also the calculated splitting of the Pt4f doublet at 3.36 eV. All these three peaks at the above-mentioned binding energies, unquestionably confirm that platinum is present in Pt-TiO$_2$ at the metallic state. One should notice that the reported XPS in terms of the Pt and Ti species and their reduced and oxidation

Fig. A1. X-ray photoelectron spectra (XPS) of 2.50 wt.% Pt-mesoTiO$_2$−550 °C. (a) XPS survey and (b) High-resolution XPS spectrum.

states respectively are consistent with the ones reported in Fig. 7a and b of the main text,

Appendix II. Quantum Yield Calculation in Photo-CREC Water II for Hydrogen Production.

The Quantum Yield provides photonic efficiencies in a photocatalytic reactor. An appropriate definition for the QY is the ratio of twice H_2 produced over the photons absorbed on mesoporous TiO_2 with a wavelength smaller than 415 nm (i.e. 2.99 eV), such as:

$$QY = \frac{2.Rate\ of\ H_2\ moles\ produced/s}{rate\ of\ photons\ absorbed\ by\ the\ photocatalyst\ with\ \lambda \leq \lambda o} \quad (A.1)$$

With λ_o being the wavelength that corresponds to the value of the optical band gap for the semiconductor material considered.

In order to calculate the absorbed photons by the photocatalyst, macroscopic balances as allowed in *Photo-CREC-Water II* unit, includes the measurement of [29]: a) Incident photons to the semiconductor (P_i), b) Photons transmitted by the semiconductor (P_t) and c) Photons backscattered by the semiconductor (P_{bs}).

In this regard, one can consider the calculation of the absorbed photons by the photocatalyst applying the algebraic addition of the P_i, P_t, P_{bs} ration as follows [29]:

$$P_a(t) = P_i(t) - P_t(t) - P_{bs}(t) \quad (A.2)$$

With the units of all these terms being in photons/s.

The Quantum Yield calculation Eq. (A.1), in the denominator accounts for radiation variation in each location of the r, θ and λ axis as follows:

$$P_a = \frac{\int_{\lambda_{min}}^{\lambda_0} \int_0^\infty \int_0^{2\pi} q(\theta, z, \lambda) r d\theta dz d\lambda}{\bar{E}} \quad (A.3)$$

where $\bar{E}$ is the average energy of a photon at a wavelength range, J/mol photon.

The near-UV lamp spectrum was characterized as reported in Fig. A2 using a spectrophotoradiometer.

Fig. A2 reports the measurements of radiation distribution in the *Photo-CREC-Water II* Reactor. These measurements were carried out to calculate the total absorbed radiation using Eq. (A.2) and subsequently to evaluate the quantum yield with Eq. (A.3).

Hence, the Quantum Yield is calculated taken in account the considerations of Eq. (A.3). Thus, the Eq. (2) converts to Eq. (A.4),

$$QY = \frac{2 \frac{dH^\bullet}{dt}}{\frac{\int_{\lambda_{min}}^{\lambda_0} \int_0^\infty \int_0^{2\pi} q_a(\theta, z, \lambda) r d\theta dz d\lambda}{\bar{E}}} \quad (A.4)$$

where q_a accounts for the absorbed radiation in $\mu W/cm^2$. The denominator is calculated using macroscopic balances as described in Eq. (A.2). Integrals of the radiation in Eq. (4) were calculated with experimentally obtained data

As an illustration of this calculation, one can considers the hydrogen evolution rate exhibited by the 2.50 wt.%-Pt-TiO_2-Meso–550 °C as 0.117 μmol H_2/cm^3 h, V_g volume of the gas phase in the storage tank as 5716 cm^3 [36], $P_a = 9.89 \times 10^{17}$ photons/s, $N_A = 6.022 \times 10^{23}$/mol H_2, the quantum yield (QY) can be calculated as follows:

$$QY = \frac{2 * \frac{0.117 \times 10^{-6} mol H_2}{cm^3 h} * 5716 cm^3 * \frac{6.022 \times 10^{23}}{mol H_2} * \frac{1h}{3600s}}{\frac{9.89 \times 10^{17} photons}{s}}$$

$$X\ 100\% = 22.6\%$$

Thus, on this basis one can conclude that the QY for the 2.50 wt.%-Pt-TiO_2-Meso–550 °C in the present article reaches the 22.6% value.

References

[1] S. Mao, S. Shen, L. Guo, Nanomaterials for renewable hydrogen production: storage and utilization, Prog. Nat. Sci.: Mater. Int. 22 (2012) 522–534.

[2] D. Jing, L. Guo, L. Zhao, X. Zhang, H. Liu, M. Li, S. Shen, G. Liu, X. Hu, Efficient solar hydrogen production by photocatalytic water splitting: From fundamental study to pilot demonstration, Int. J. Hydrogen Energy 35 (2010) 7087–7097.

[3] P. Häussinger, R. Lohmüller, A. Watson, Hydrogen, 1. properties and occurence, Ullmann's Encycl. Ind. Chem. (2011) 1–15.

[4] Y. Navarro, M.C. Rufino, M. Álvarez-Galván, F. Del Valle, J.A. Villoria De La Mano, J.L.G. Fierro, Water splitting on semiconductor catalysts under visible-light irradiation, ChemSusChem 2 (2009) 471–485.

[5] R.M. Navarro, F. Del Valle, J.A. Villoria De La Mano, M.C. Álvarez-Galván, J.L.G. Fierro, Photocatalytic water splitting under visible light: concept and catalysts development: photocatalytic technologies, Adv. Chem. Eng. 36 (2009) 111–143.

[6] K. Maeda, K. Teramura, D. Lu, T. Takata, S. Inoue, K. Domen, Photocatalyst releasing hydrogen from water, Nature 440 (2006) 295.

[7] K. Nakata, A. Fujishima, TiO2 photocatalysis: design and applications, J. Photochem. Photobiol. C: Photochem. Rev. 13 (2012) 169–189.

[8] J. Nowotny, C.C. Sorrell, L.R. Sheppard, T. Bak, Solar-hydrogen. 1, environmentally safe fuel for the future, Int. J. Hydrogen Energy 30 (2005) 521–544.

[9] U.S. Department of Energy, Hydrogen production Fuel Cells and Infrastructure Technologies Program, vol. 3, 2009, pp. 1–20.

[10] K. Honda, A. Fujishima, Electrochemical evidence for the mechanism of the primary stage of photosynthesis, Bull. Chem. Soc. Jpn. 44 (1971) 1148–1150.

[11] K. Honda, A. Fujishima, Electrochemical photolysis of water at a semiconductor electrode, Nature 238 (1972) 37–38.

[12] P. Du, J. Schneider, F. Li, W. Zhao, U. Patel, F.N. Castellano, R. Eisenberg, Bi- and terpyridyl platinum(II) chloro complexes: molecular catalysts or the photogeneration of hydrogen from water or simply precursors for colloidal platinum, J. Am. Chem. Soc. 130 (2008) 5056–5058.

[13] P. Lei, M. Hedlund, R. Lomoth, H. Rensmo, O. Johansson, L. Hammarstrom, The role of colloid formation in the photoinduced H2 production with a RuII-PdII supramolecular complex a study by GC XPS, and TEM, J. Am. Chem. Soc. 130 (2008) 26–27.

[14] K. Domen, S. Naito, M. Soma, T. Onishi, K.J. Tamaru, Chem. Soc. Chem. Commun. 12 (1980) 543–544.

[15] S. Sato, J.M. White, Chem. Phys. Lett. 72 (1980) 83–86.

[16] J.M. Lehn, J.P. Sauvage, R. Ziessel, NouV. J. Chim. (1980) 4623–4627.

[17] K. Domen, S. Naito, T. Onishi, K. Tamaru, Chem. Phys. Lett. 92 (1982) 433–434.

[18] K. Sayama, H.J. Arakawa, Phys. Chem. 97 (1993) 531–533.

[19] Y. Inoue, T. Kubokawa, K. Sato, Photocatalytic activity of sodium hexatitanate, $Na_2Ti_6O_{13}$, with a tunnel structure for decomposition of water, J. Chem. Soc. Chem. Commun. 19 (1990) 1298–1299.

[20] Y. Inoue, T. Niiyama, T. Asai, K. Sato, Stable photocatalytic activity of BaTi4O9 combined with ruthenium oxide for decomposition of water, J. Chem. Soc. Chem. Commun. (1992) 579–580.

[21] S. Ikeda, T. Itani, K. Nango, M. Matsumura, Catal. Lett. 98 (2004) 229–233.

[22] T. Takata, Y. Furumi, K. Shinohara, A. Tanaka, M. Hara, J.N. Kondo, K. Domen, Chem. Mater. 9 (1997) 1063–1064.

[23] S. Ikeda, M. Hara, J.N. Kondo, K. Domen, H. Takahashi, T. Okubo, M.J. Kakihana, Mater. Res. 13 (1998) 852–855.

[24] A. Kudo, H. Kato, Chem. Lett. 26 (1997) 867–877.

[25] H.G. Kim, D.W. Hwang, J. Kim, Y.G. Kim, J.S. Lee, Chem. Commun. 107 (1999) 7–1078.

[26] J. Cerdá, J.L. Marchetti, A.E. Cassano, Radiation efficiencies in elliptical photoreactors, Lat. Am. J. Heat Mass Transfer 1 (1977) 33–63.

[27] H. Ibrahim, H. de Lasa, Photo-catalytic degradation of air borne pollutants. Apparent quantum efficiencies in a novel photo-CREC-air reactor, Chem. Eng. Sci. 58 (2003) 943–949.

[28] H. Ibrahim, Photo-catalytic Reactor for the Degradation of Airborne Pollutants: Photo-conversion Efficiency and Kinetics Modeling, The University of Western Ontario, London, Canada, 2001, Ph.D. dissertation.

[29] H. de Lasa, B. Serrano, M. Salaices, Photocatalytic Reaction Engineering, first ed., Springer, New York, 2005.

[30] M.R. Hoffmann, S.T. Martin, W. Choi, Environmental applications of semiconductor photocatalysis, Chem. Rev. 95 (1995) 69–77.

[31] H. Tahiri, N. Serpone, R. Le Van Mao, Application of concept of relative photonic efficiencies and surface characterization of a new titania photocatalyst designed for environmental remediation, Photochem. Photobiol. A: Chem. 93 (1996) 199–203.

[32] H. Kisch, On the problem of comparing rates or apparent quantum yields in heterogeneous photocatalysis, Angew. Chem. Int. Ed. 49 (2010) 9588–9589.

[33] S. Escobedo-Salas, B. Serrano-Rosales, H. de Lasa, Quantum Yield in a Photo-CREC reactor for hydrogen production, AIChE Annual Meeting (2012).

[34] J. Moreira, B. Serrano, A. Ortiz, H. de Lasa, TiO$_2$ absorption and scattering coefficients using Monte Carlo method and macroscopic balances in a photo-CREC unit, Chem. Eng. Sci. 66 (2011) 5813–5852.

[35] B. Serrano, A. Ortiz, J. Moreira, H. de Lasa, Energy efficiency in photocatalytic reactors for the full span of reaction times, Ind. Eng. Chem. Res. 48 (2009) 9864–9876.

[36] S. Escobedo-Salas, B. Serrano-Rosales, H. de Lasa, Quantum yield with platinum modified TiO2 photocatalyst for hydrogen production, Appl. Catal.–B Environ. 140 (2013) 523–536.

[37] P.J. Valadés-Pelayo, J. Moreira, P. Solano-Flores, Benito Serrano, Hugo De Lasa, Establishing photon absorption fields in a Photo-CREC Water II Reactor using a CREC-spectroradiometric probe, Chem. Eng. Sci. 116 (2014) 406–417.

[38] Swapan K. Das, Manas K. Bhunia, Asim Bhaumik, Self-assembled TiO$_2$ nanoparticles: mesoporosity, optical and catalytic properties, R. Soc. Chem. Dalton Trans. 39 (2010) 4382–4390.

[39] C.C. Nguyen, N.-N. Vu, Trong-On Do, Recent advances in the development of sunlight-driven hollow structure photocatalysts and their applications, J. Mater. Chem. A 7 (2015) 8187–8208, Review Article.

[40] M. Reza Gholipour, C.-T. Dinh, F. Beland, Trong-On Do, Nanocomposite heterojunctions as sunlight-driven photocatalysts for hydrogen production from water splitting, Nanoscale 7 (2015) 8187–8208, Review Article.

[41] C.-T. Dinh, Y. Hoang, F. Kleitz, Trong-On Do, Three-dimensional ordered assembly of thin-shell Au/TiO$_2$ hollow nanospheres for enhanced visible-light driven photocatalysis, Angew. Chem. Int. Ed. Engl. (53) (2014) 6618–6623.

[42] C.-T. Dinh, M.-H. Pham, Y. Seo, F. Kleitz, Trong-On Do, Design of multicomponent photocatalysts for hydrogen production under visible light using water-soluble titanate nanodisks, Nanoscale 6 (9) (2014) 4819–4829.

[43] X. Wang, J.C. Yu, H.Y. Yip, L. Wu, P.K. Wong, S.Y. Lai, A mesoporous Pt/TiO$_2$ nanoarchitecture with catalytic and photocatalytic functions, Chem. Eur. J. 11 (2005) 2997–3004.

[44] Chih-Chieh Chan, Chung-Chieh Chang, Wen-Chia Hsu, Shih-Kai Wang, Jerry Lin, Photocatalytic activities of Pd-loaded mesoporous TiO2 thin films, Chem. Eng. J. 152 (October (2–3)) (2009) 492–497.

[45] Yan-Feng Zhu, Lu Xu, Juan Hu, Juan Zhang, Rong-Gui Du, Chang-Jian Lin, Fabrication of heterostructured SrTiO3/TiO2 nanotube array films and their use in photocathodic protection of stainless steel, Electrochim. Acta 121 (1) (2014) 361–368.

[46] Weijiong Dai, Junqing Yan, Ke Dai, Landong Li, Naijia Guan, Ultrafine metal nanoparticles loaded on TiO2 nanorods: synthesis strategy and photocatalytic activity, Chin. J. Catal. 36 (11) (2015) 1968–1975.

[47] Chapter 6: diodes, in: Fundamentals of Electrical Engineering, 2nd ed., Oxford UP, New York, New York, 1996, pp. 352–354, Print.

[48] R. Borja-Urby, L.A. Diaz-Torres, I. Garcia-Martinez, D. Bahena-Uribe, Gilberto Casillas, A. Ponce, M. Jose-Yacaman, Crystalline and narrow band gap semiconductor BaZrO3: Bi–Si synthesized by microwave–hydrothermal synthesis, Catal. Today 250 (July) (2015) 95–101.

[49] Shamsa Munir, Syed Mujtaba Shah, Hazrat Hussain, Rafaqat Ali Khan, Effect of carrier concentration on the optical band gap of TiO$_2$ nanoparticles, Mater. Des. 92 (February) (2016) 64–72, ISSN 0264-1275.

[50] E. Barajas-Ledesma, M.L. García-Benjume, I. Espitia-Cabrera, M. Ortiz-Gutiérrez, F.J. Espinoza-Beltrán, J. Mostaghimi, M.E. Contreras-García, Determination of the band gap of TiO$_2$–Al$_2$O$_3$ films as a function of processing parameters, Mater. Sci. Eng.: B 174 (October (1–3)) (2010) 71–73.

[51] Aaron Ortiz-Gomez, Benito Serrano-Rosales, Jesus Moreira-del-Rio, Hugo de-Lasa, mineralization of phenol in an improved photocatalytic process assisted with ferric ions: reaction network and kinetic modeling, in: Hugo I. de Lasa, Benito Serrano Rosales (Eds.), Advances in Chemical Engineering, vol. 36, Academic Press, 2009, pp. 69–110.

[52] P.J. Valadés-Pelayo, Jesus Moreira del Rio, Pastor Solano-Flores, B. Serrano, H. de Lasa, Establishing photon absorption fields in a Photo-CREC Water II Reactor using a CREC-spectroradiometric probe, Chem. Eng. Sci. 116 (6) (2014) 406–417.

[53] P.J. Valades-Pelayo, J. Moreira, B. Serrano, H. de Lasa, Boundary conditions and phase functions in a Photo-CREC Water-II reactor radiation field, Chem. Eng. Sci. 107 (April) (2014) 123–136.

[54] P.J. Valadés-Pelayo, F. Guayaquil Sosa, B. Serrano, H. de Lasa, Eight-lamp externally irradiated bench-scale photocatalytic reactor: scale-up and performance prediction, Chem. Eng. J. 282 (15) (2015) 142–151.

[55] K.S.W. Sing, D.H. Everett, R.A.W. Haul, L. Moscou, R.A. Pierotti, J. Rouquerol, T. Siemieniewska, Reporting physisorption data for gas/solid systems with special reference to the determination of surface area and porosity, Pure Appl. Chem. 57 (1985) 603–619.

[56] J.C.P. Broekhoff, Mesopore determination from nitrogen sorption isotherms: fundamentals, scope, limitations, Stud. Surf. Sci. Catal. 3 (1979) 663–684.

[57] J.E. Shields, S. Lowell, M.A. Thomas, M. Thommes, Characterization of Porous Solids and Powders: Surface Area, Pore Size and Density, Kluwer Academic Publisher, Boston, MA, USA, 2004, pp. 43–45.

[58] Z.A. ALOthman, A. Review, Fundamental aspects of silicate mesoporous materials, Materials 5 (2012) 2874–2902.